Insight into the synergistic effect of adsorption and photocatalysis for the removal of organic dye pollutants by novel BiFeO$_3$@GO fibers

Ze Du[1] , Yanmei Li[1], Daihong Kuang[2,*] , Wenquan Wang[1], Fangyuan Yang[2,*], Jiadong Yang[2], and Liang Hou[1]

[1] *School of Resources and Environment, Xinjiang Agricultural University, Ürümqi 830052, Xinjiang Uygur, China*
[2] *School of Mathematics and Physics, Xinjiang Agricultural University, Ürümqi 830052, Xinjiang Uygur, China*

ABSTRACT

BiFeO$_3$@GO nanocomposite fibers were successfully synthesized by the electrospinning and simple ultrasound method. The structure, morphology, optical, composition and magnetic properties of BiFeO$_3$@GO samples were characterized by XRD, FT-IR, SEM, TEM, UV–Vis and XPS analyses. The results showed that the removal of organic dye pollutants was enhanced by novel BiFeO$_3$@GO fibers through the adsorption–photocatalytic synergy. The removal rates of methylene blue (MB), Congo red (CR), Rhodamine B (RHB) and norfloxacin (NOR) dyes were increased by 64.5%, 33.6%, 43% and 61.1%, respectively. Then it was a benefit to remove MB when the pH is between 6.0 and 10.0, while it was favorable for adsorption in a neutral environment and photocatalysis in an acidic or alkaline environment. The adsorption process of MB dyes was more in line with the pseudo-second-order kinetic model for BiFeO$_3$@GO nanocomposite sample with 3 mg graphene oxide weight (GO$_3$). The adsorption data were well fitted by Langmuir adsorption isotherm, which indicated that the adsorption process was a monolayer adsorption. The adsorption of MB dyes on GO$_3$ nanocomposite fibers appeared to be a favorable process ($0 < R_L < 1$). Moreover, the trapping experiments showed that ˙OH was the main active substance during photocatalysis, and the FT-IR tests indicated that nanocomposite fibers can degrade MB into CO$_2$ and H$_2$O under the synergistic effect of adsorption and catalysis.

Address correspondence to E-mail: 416799621@qq.com; 287217510@qq.com

Springer

1 Introduction

There is no life without water. All life activities require the support of fresh water, but most of the earth's freshwater is in glaciers and underground, and only a small amount of water (0.29–0.49%) is available for drinking [1]. Many countries in the world are facing water resource shortages [2]. Unfortunately, with the rise of industrialization, many rivers and lakes are polluted due to the excessive use of dyes in textile coloring [3]. These sewage contain toxic, carcinogenic and mutagenic substances that lead serious pollution to the water environment [4, 5]. Moreover, these hazardous organic dyes are almost non-biodegradable, so the removal of organic dyes from wastewater is essential for human health [6, 7]. How to effectively treat all kinds of textile dyes has become an urgent problem [8]. Membrane separation [9, 10], adsorption [11, 12], photocatalysis [13], flocculation [14–16] and photo-Fenton techniques [17–19] have been reported by scholars. Adsorption is a simple, efficient, and low-cost method, which is favored by many researchers [20]. The adsorbent can effectively adsorb pollutants by utilizing its high specific surface area, large porosity, good pore structure, and a large number of oxygen-containing functional groups [21, 22]. Carbon materials have been widely used as the traditional and most abundant adsorbents. And the porous carbon materials commonly used to study dye adsorption mainly include activated carbon, AC [23], graphene oxide, GO [24], carbon nanotube [25] and biomass carbon [26].

However, pollutants adsorbed by the adsorbent are concentrated on the material's surface, and the organic pollutants cannot be thoroughly degraded, which is easy to cause secondary pollution [27]. Therefore, this has attracted much attention to cleaner photocatalytic technologies for degrading various organic pollutants. Photocatalysis is a promising and environmentally friendly technology [28]. In fact, photocatalysis as an advanced oxidation process (AOP) can perform electronic transition motion by absorbing solar radiation energy (ultraviolet light and visible light). And then this motion can generate substances with strong oxidizing and reducing properties, which can degrade organic pollutants into CO_2 and H_2O completely [29, 30].

An antiferromagnetic and ferroelectric property of bismuth ferrite ($BiFeO_3$, BFO) makes it a good photocatalytic material for visible light. Besides, it has a rhombohedral structure with a $R3c$ space group at room temperature [31].Compared with TiO_2 that can only absorb UV light, BFO can occur photocatalytic reactions in the visible light region due to its narrow band gap (2.2 eV), and its unique magnetism makes recycling possible [32, 33]. However, the high recombination rate of photogenerated electrons (e^-) and holes (h^+) in pure BFO limits its further application as a photocatalyst in wastewater degradation [34]. Therefore, researchers mainly change the forbidden band width of BFO through ion doping [35], semiconductor composite [36], and noble metal deposition [37] to reduce the recombination rate of electron–hole pairs, which is very important to improve the photocatalytic effect.

As an emerging two-dimensional (2D) material, GO has become a research hotspot in recent years and has been applied in many aspects [38]. Further, the GO can exhibit good adsorption properties due to its larger surface area, superior biocompatibility, strong chemical and thermal stability. Not only that, GO contains oxygen-rich functional groups [(–COOH), (C–O–C), (–OH) and (C=O)] on its basal plane and edges, which are very beneficial to eliminate pollutants in wastewater [39, 40]. In addition, GO has been gradually applied in photocatalytic research because of its unique transport properties, high mechanical strength, high carrier mobility, high electrical conductivity and other fascinating properties [41]. The composition of GO as a zero-bandgap material with photocatalysts is considered to be the most promising strategy [42, 43]. The pollutants in water are first adsorbed on the surface of the adsorbent and then degraded by a photocatalytic process. This synergistic method can potentially address the secondary pollution of adsorption and the high recombination rate of e^-–h^+ pairs during photocatalytic degradation [44].

In conclusion, taking advantage of the strong adsorption property of GO and the photocatalytic property of BFO in the paper, a new BFO@GO nanocomposite material with adsorbable and photocatalytic properties was successfully prepared by a simple ultrasonic method. At the same time, the morphology, chemical composition, valence state, optical properties and other changes of the composite materials were studied. Finally, adsorption characteristics and photocatalytic mechanism of the

composite materials were further researched in the process of degrading dyes.

2 Materials and methods

2.1 Materials

$Fe(NO_3)_3 \cdot 9H_2O$ ($\geq 98\%$), $Bi(NO_3)_3 \cdot 5H_2O$ ($\geq 98\%$), ethylene glycol monomethyl ether, *tert*-butanol (TBA, $\geq 98\%$), glacial acetic acid, *N*, *N*-dimethylformamide, anhydrous ethanol, PVP, and ammonium oxalate (AO, $\geq 98\%$) were obtained from Aladdin. HCl (60–65%), NaOH ($\geq 98\%$), GO, Congo red (CR), norfloxacin (NOR), methylene blue (MB) and Rhodamine B (RHB) were obtained from Macklin Biochemical. All the chemicals in this research were used as received without additional purification.

2.2 Fabrication of BiFeO₃ fibers and BiFeO₃@GO nanocomposite

0.2 mol/L $Bi(NO_3)_3 \cdot 5H_2O$ (Bi was volatile near the crystallization temperature, so 5% Bi ion was added in excess [45, 46]) and 0.2 mol/L $Fe(NO_3)_3 \cdot 9H_2O$ were dissolved in 5 mL ethylene glycol methyl ether with the assistance of ultrasound, and 3 mL glacial acetic acid was added to adjust the consistency of the solution, as A solution. In addition, 7.5 mL *N*, *N*-dimethylformamide was accurately measured and mixed with 4.5 mL absolute ethanol. The concentration of PVP was controlled at about 9%, which had a better spinning effect. The mixture was stirred thoroughly until colorless and transparent, as solution B. A uniform BFO precursor solution was formed after mixing and stirring the A and B solutions for 12 h. And the pre-spinning solution was put into a 5 mL syringe. Then the temperature and humidity were controlled, and a uniform fiber film was spun out under the conditions of a voltage of 13 kV and a pushing speed of 0.001 mL/s. The prepared fiber film was calcined in a Muffle furnace at 550 °C for 2 h, and the heating rate was 5 °C/min to obtain pure BFO, as shown in Fig. 1a.

As shown in Fig. 1b, to assemble BFO nanofibers on GO flakes, the pure BFO and GO sheets were dissolved in 5 mL of ethanol solvent and sonicated for 60 min, until BFO fibers and GO sheets were dispersed entirely. Then, the homogeneous solution of BFO and GO was dried at 80 °C for 12 h to prepare BiFeO₃@GO nanocomposites. The BiFeO₃@GO nanocomposites with GO weights of 1 mg, 3 mg, and 5 mg were denoted as "GO₁", "GO₃" and "GO₅", respectively.

2.3 Characterization

To examine the morphology, a scanning electron microscope (SEM, Zeiss Sigma 300) was used. And TEM (FEI Talos F200x) with EDX attachment was used to detect the nanocomposite fiber fine structure and elemental composition. The crystal structure of the nanocomposite fibers was investigated using X-ray diffraction (XRD, Bruker D8 Advance). The optical characteristics of the nanocomposite fibers was investigated by UV–Vis diffuse reflection spectroscopy (UV–Vis DRS, PerkinElmer Lambda1050). X-ray photoelectron spectroscopy (XPS, Thermo Scientific K-Alpha) was used to determine the elemental composition and electronic states of the nanocomposite fibers. The Fourier transform infrared spectrum (FT-IR, Thermo Nicolet iS 10) was used to detect functional group of the material and MB dyes degradation.

3 Results and discussion

Figure 2a shows the XRD patterns of BFO nanocomposite with different GO loadings. All the diffraction peaks are well-matched with the PDF standard card (JCPDS card no. 70-2035). The peaks at $2\theta = 22.45°$, 31.8°, 32°, 39°, 39.5°, 45.8°, 51.4°, 51.8°, 56.5°, 57° and 57.2° are correspond to (012), (104), (110), (006), (202), (024), (116), (122), (018), (214) and (300) plane of BFO, respectively. These diffraction peaks prove that the prepared pure BFO and BiFeO₃@GO nanocomposites have a rhombohedral structure with space group *R3c*. In addition, the added different quantities of GO do not change the crystal structure of BFO [47, 48]. Figure 2b shows the partial enlarged view of $2\theta = 9.5°$–15.5°. It can be clearly observed that a new diffraction peak appears at about 11.2° after the addition of GO, which belongs to the characteristic peak of GO [49]. As the composition of GO increases, the characteristic peak intensity of GO was gradually increased, which indicates that GO and BFO are successfully combined and exhibit good crystallinity. In addition, as a metastable structure, the synthesis of BFO is always accompanied by some secondary
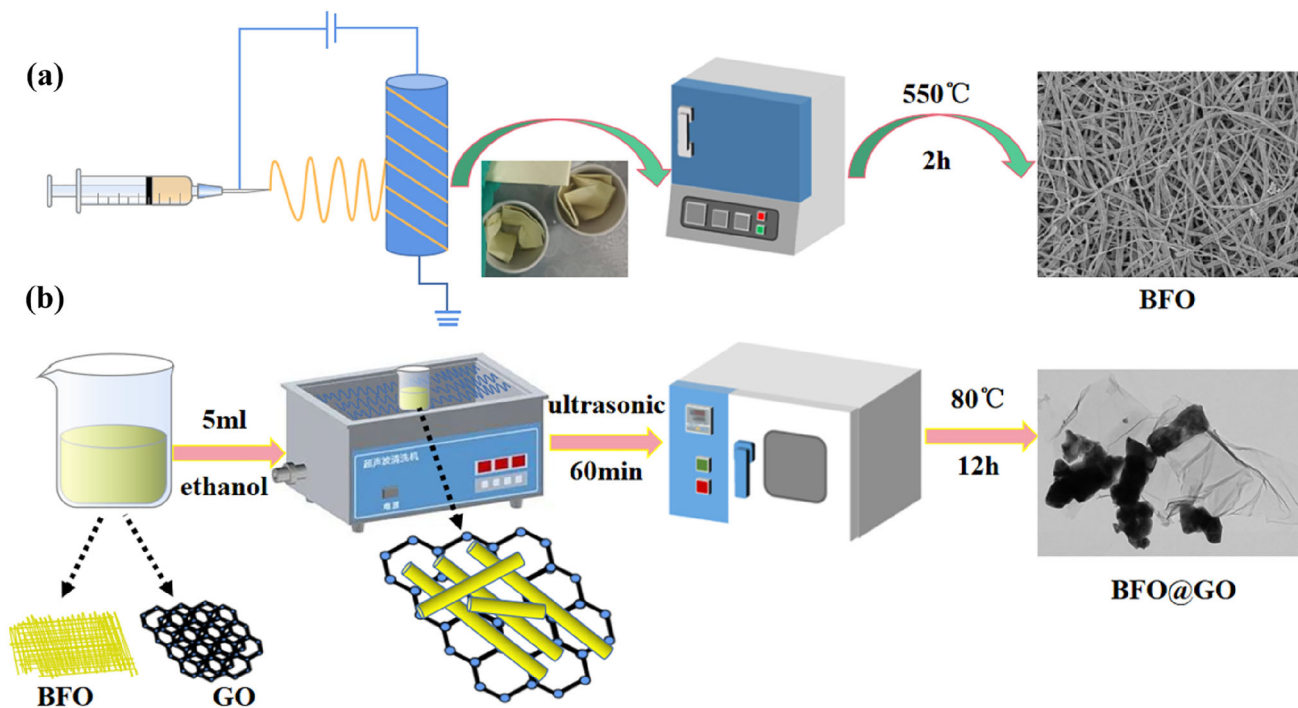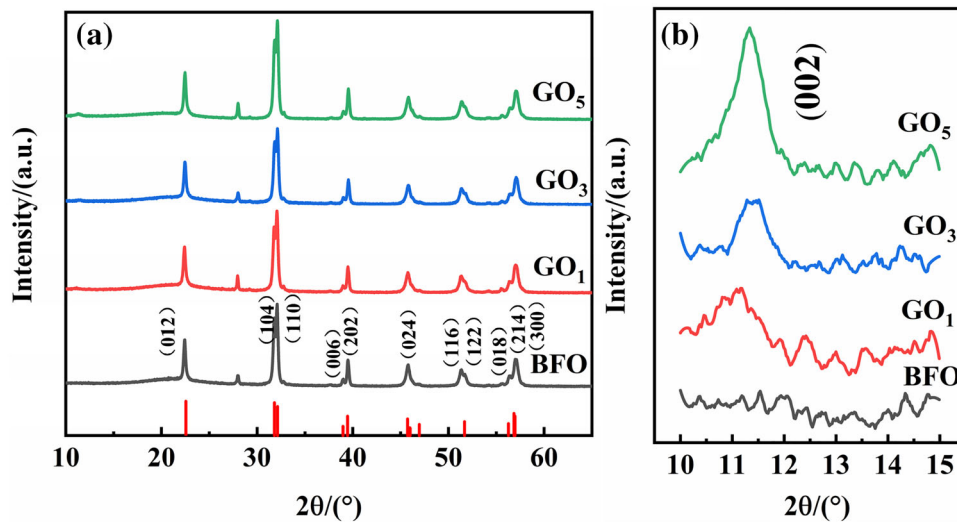
Fig. 1 Schematic depiction for the synthesis of BFO fibers and BFO@GO nanocomposite

Fig. 2 XRD patterns of **a** BFO, GO_1, GO_3 and GO_5, and **b** $2\theta = 9.5°–15.5°$

phases such as $Bi_2Fe_4O_9$ [50], Bi_2O_3 [51] and $Bi_{25}FeO_{39}$ [52]. Due to the kinetics of phase formation [53], a small amount of impurity phase (Bi_2O_3, $2\theta \approx 27.9°$) was observed in both pure BFO and $BiFeO_3$@GO nanocomposites.

In Fig. 3, SEM morphological features of BFO and GO_3 are depicted. It can be found that the pure BFO have a continuous fiber structure with uniform size and good spinning effect from Fig. 3a, b. The fiber structure of GO_3 nanocomposite still keeps intact and

the fiber skeleton is integrity in Fig. 3c, d. Also, long continuous fibers are broken and recombined into a compact aggregated structure. From the inset of Fig. 3a, c, the average particle size of BFO fibers is 0.25 nm, but the particle size distribution of GO_3 nanocomposite is more concentrated in the range of 0.2–0.3 nm. This phenomenon may be related to the reverse Ostwald ripening process [54–56]. Due to BFO fiber skeleton was broken and dispersed into solution under high power ultrasonic state, and the
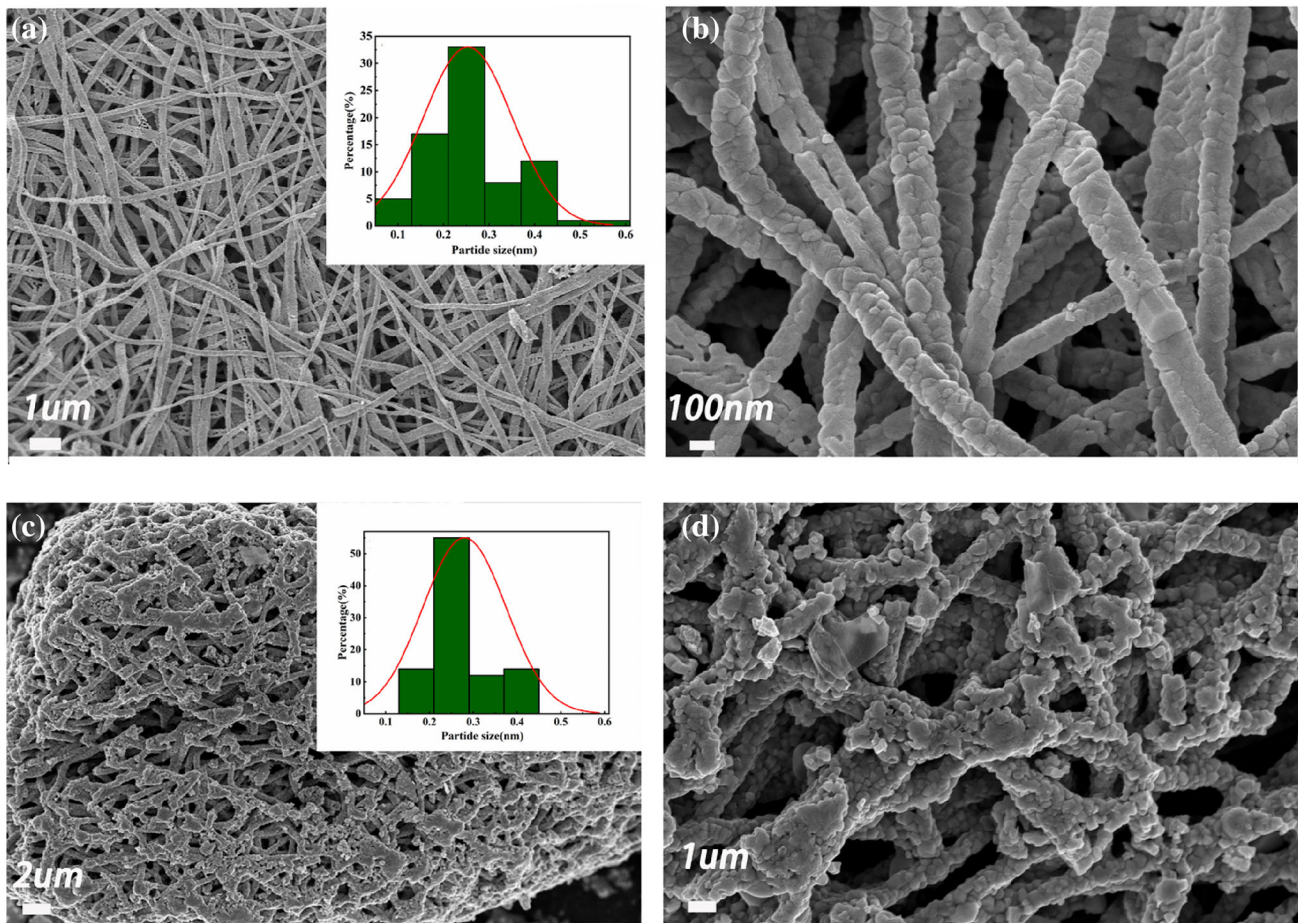
Fig. 3 **a** SEM particle size distribution image of BFO, **b** SEM images of BFO, **c** SEM particle size distribution image of GO$_3$, and **d** SEM images of GO$_3$

structure is reorganized into tiny droplets with BFO fibers coated in solution. After ultrasonic treatment, ethanol evaporates when it was heated up and the tiny droplets were rapidly deposited and then formed a unique fiber skeleton that supported each other, but there were no obvious GO peaks observed in the figure.

Microstructure of GO$_3$ nanocomposite was further investigated by TEM. Figure 4a shows that BFO fibers and GO monolayer were tightly integrated. In Fig. 4b, the interplanar spacing of GO$_3$ is 0.27 nm, which corresponds to (110) lattice plane of BFO in XRD diagram. The presence of lattice planes suggested that well-developed nanocrystallite of GO has existed in the nanocomposite [57, 58]. Figure 5a–d shows that the element analysis of GO$_3$ sample was scrutinized by EDX mapping. From the element distribution diagram, it can be seen that the sample contains Bi, Fe, and O elements. It should be noted

that C element of the GO can also be well displayed. Thus, it demonstrated that BFO and GO have been successfully recombined.

BiFeO$_3$ is a narrow band gap metal oxide semiconductor for photocatalytic materials [59]. In order to evaluate its optical properties, the UV–Vis diffuse reflection measurement was used to explore the effects of GO composition on the band gap and light absorption capacity of BFO. In Fig. 6a, BFO has strong light absorption in the range of 200–500 nm, but the absorption drops sharply above 500 nm. As the wavelength range of visible light is 400–760 nm, the application of BFO as an efficient visible light photocatalyst was limited due to the limited absorption of visible light. But GO$_3$ nanocomposite showed better light absorption in the ultraviolet and visible light range compared with BFO. It indicates that the light absorption performance of BFO under visible light was significantly improved after combining
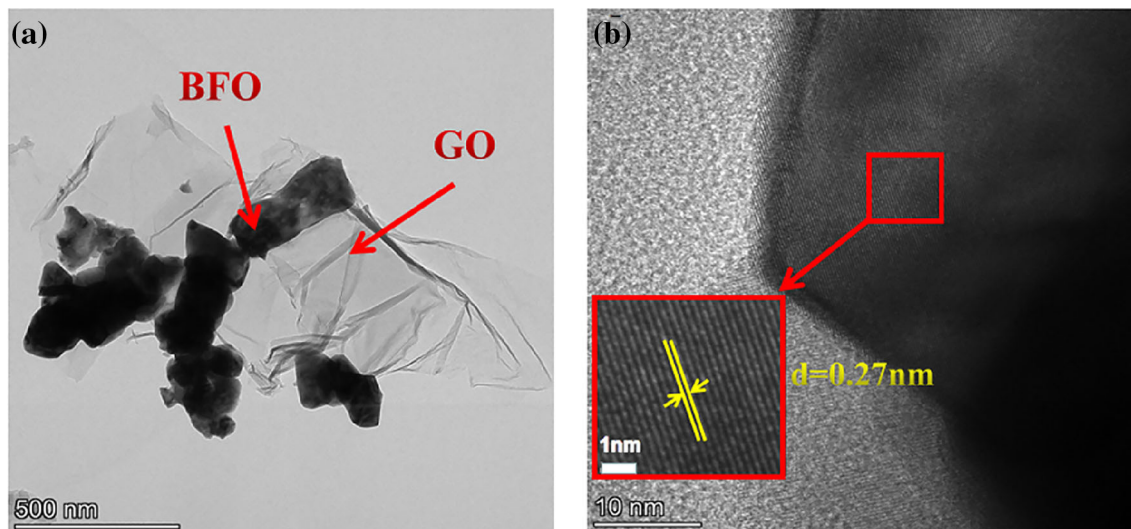
Fig. 4 TEM image of **a** and **b** GO₃ nanocomposite

with GO. Accordingly, GO₃ composite can generate more photogenerated electron–hole pairs if it has stronger light absorption [60]. From the Tauc's Eq. (1) and Fig. 6b, the corresponding bandgap widths of GO₃ and BFO were estimated to be 1.90 eV and 1.95 eV, which were consistent with the previously reported BiFeO₃/reduced GO [61]. The coexistence of GO and BiFeO₃ may explain the improved optical properties and decreased bandgap of the GO₃.

$$\alpha h v = C(h v - E_g)^{1/2}. \tag{1}$$

In this equation, C is a constant, h is Planck's constant, v is the incident photon frequency, α is the absorption coefficient, and E_g is the band gap value.

XPS was used to analyze the surface chemical composition, oxidation state, and valence state of BFO and GO₃ samples. As shown in Fig. 7a, the XPS spectra of GO₃ and BFO indicate that the main elements of the prepared samples contain Bi, Fe, O and C. The peak of pure BFO was obtained by the C 1s peak correction at 284.8 eV. The C content in the pure BFO was 40.95% and the O content was 33.23%. The C/O ratio was 1.232; the C content in GO₃ was 49.06%, and the O content was 35.97%. The C/O ratio was 1.363. The amounts of O and C were significantly increased in GO₃ compared to pure BFO. In Fig. 7b, 284.47, 286.72 and 287.94 eV represent C–C, C–O, and COOH/O = C in the C 1s fitted peak of GO₃, respectively [62, 63]. Figure 7c shows the high-resolution spectra of O 1s for BFO and GO₃ samples. The fitted peaks of binding energies at 528.89 and 529.78 eV for O 1s in BFO correspond to Bi–O bonds and Fe–O bonds, respectively. While the peak with binding energy of 531.09 eV is related to oxygen vacancies. Similar conclusions have been got by other scholars [64, 65]. However, the metal lattice oxygen and oxygen vacancies of O 1s in GO₃ shift to 529.77 and 531.89 eV. The new highest fitting peak at 532.46 eV belongs to COOR. Perhaps this is related to oxygen-containing functional groups in GO [56]. Two characteristic peaks of Fe 2p appeared at 710.86 and 724.18 eV for BFO correspond to Fe 2p₃/₂ and Fe 2p₁/₂ in Fig. 7d, respectively [66]. The satellite peak between Fe 2p₃/₂ and Fe 2p₁/₂ is 7.22 eV more than the peak of Fe 2p₃/₂ (usually 6–8 eV more than Fe 2p₃/₂ peak). These characteristics indicate that the oxidation state of Fe ions is + 3 in pure BFO. The results also show that the fitting peaks of Bi 4f and Fe 2p in GO₃ shift to a higher binding energy. This may be due to the existence of GO. Figure 7e shows that two strong peaks of Bi 4f are appeared at 163.97 and 158.65 eV, belonging to Bi 4f₅/₂ and Bi 4f₇/₂ [65]. The difference between their binding energies is 5.32 eV, which provides evidence of Bi³⁺ existing in the Bi–O bond.

In order to investigate the removal capacity of BiFeO₃@GO materials for MB dyes, degradation experiments were conducted. Firstly, prepared fiber nanocomposite (0.02 g) was added into 50 mL MB solution (10 mg/L). Next, the dyes were adsorbed to the surface of the nanocomposite in dark reaction for 30 min. Finally, MB dyes were degraded by 700 W xenon lamp irradiation. During the photocatalytic
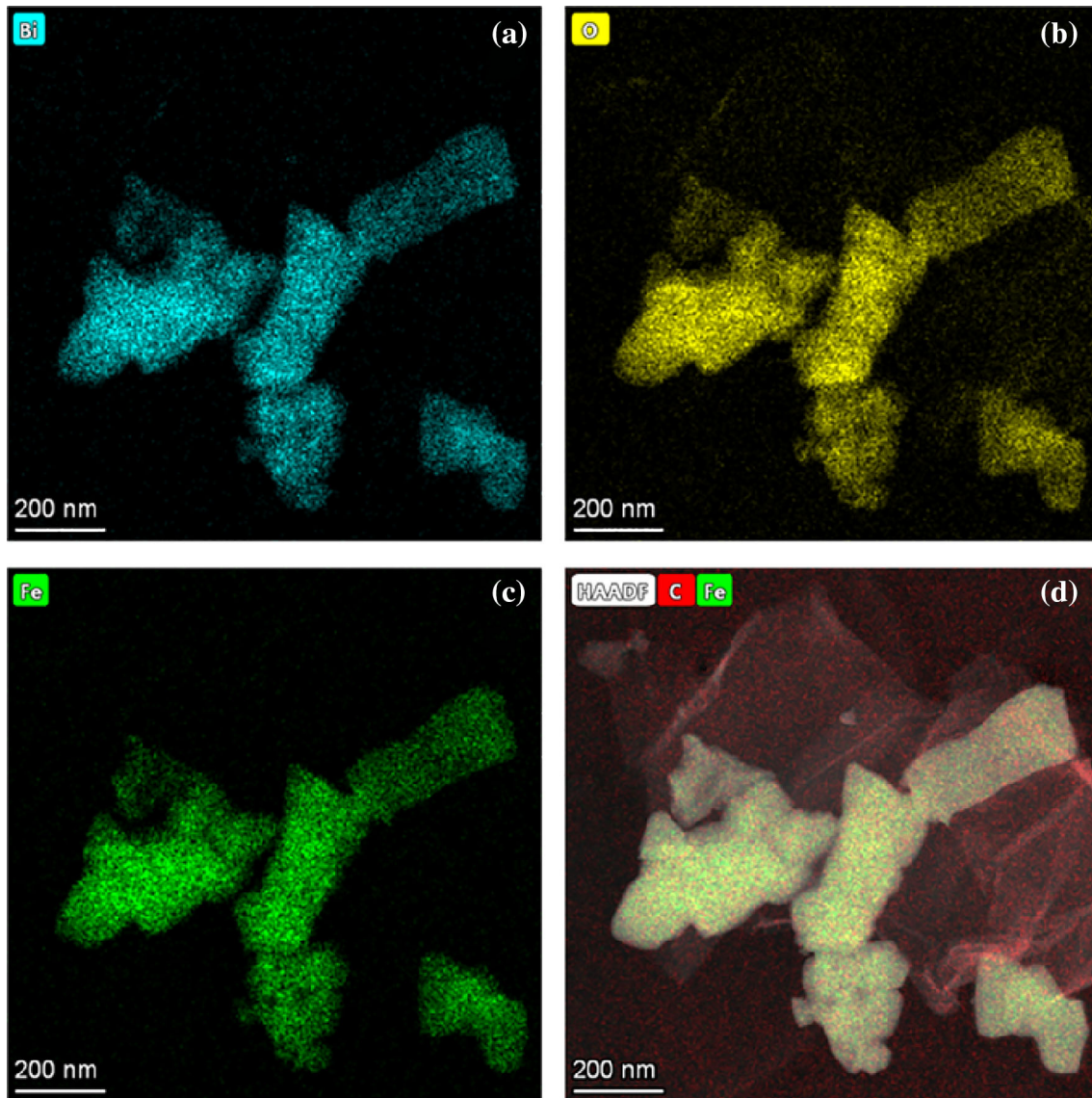
Fig. 5 EDX element maps of the corresponding area of **a** Bi, **b** O, **c** Fe and **d** C and Fe

experiment, samples were taken every 30 min for absorbance tests. As shown in Fig. 8, the degradation rates of BFO, GO_1, GO_3 and GO_5 were 24.0%, 52.6%, 94.0% and 88.5%, respectively. This revealed that GO_3 had the highest degradation rate. The degradation capacity of MB of $BiFeO_3@GO$ material has been improved in varying degrees due to the addition of GO. Compared with pure BFO, the degradation rate of MB of GO_3 was increased by 70.0%. Furthermore, GO_3 sample showed a better degradation effect of CR, RHB and NOR. As shown in Fig. 9, under a synergistic effect of adsorption and catalysis, the degradation rates of CR, RHB and NOR for GO_3 were increased by 33.6%, 43% and 61.1%, respectively.

Because the adsorption and photocatalysis occur on the surface of the material, pH is one of the most critical parameters, which affect the capacity of materials to degrade [67, 68]. Under different pH conditions, the adsorption and photocatalytic properties of GO_3 nanocomposite were shown in Fig. 10. In an acid environment, the absorption capacity of GO_3 to MB dyes was also increased with the increase of pH value. This may be the competition between H^+ and MB cationic dyes for active sites under acid conditions, which leads to decrease the adsorption effect [69]. The adsorption rate reached a maximum at pH 8. When pH > 8, the adsorption rate began to decrease. Because pH exceeds pHpzc (point of zero
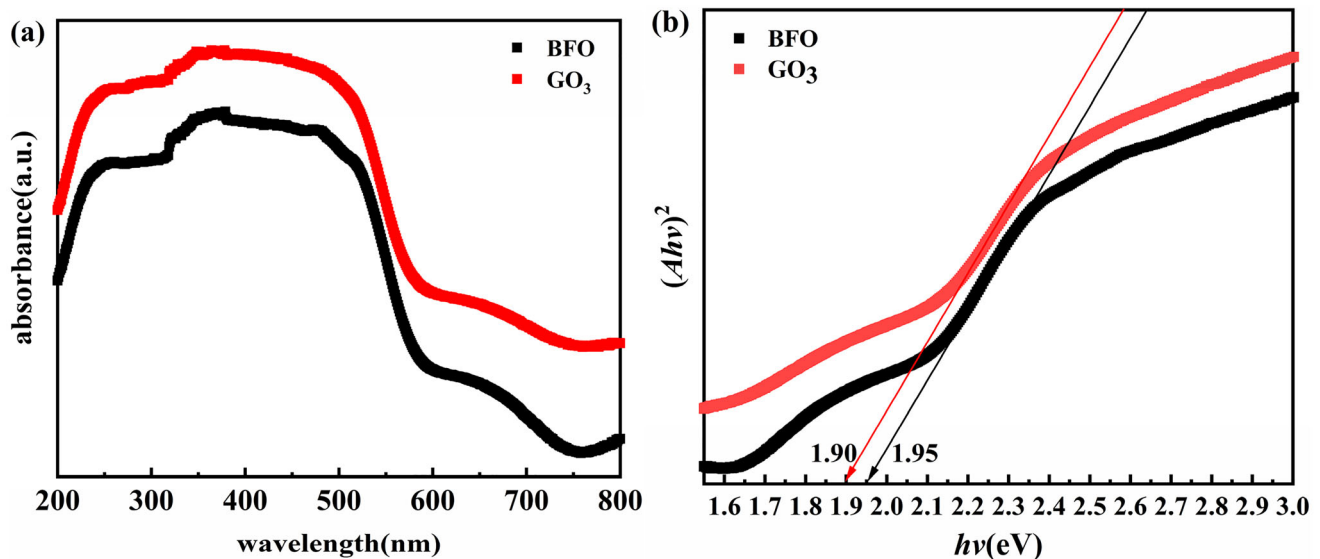
Fig. 6 a UV–Vis spectrum of BFO and GO_3 nanocomposite, and **b** $(\alpha h v)^2$ versus $h v$ curves

charge) of GO_3 in a strong alkaline environment, which makes the material surface appear negative charge. Therefore, excess OH^- can inhibit the adsorption of MB dyes [70, 71]. But the photocatalytic efficiency was the lowest when the pH is 8, it was improved in varying degrees with an acidic or a strong alkaline environment. This is because hole, superoxide anion and hydroxyl radical play main roles in the photocatalytic processes [72]. Under acidic conditions, the presence of H^+ ions favors the formation of superoxide anions. While excess OH^- favors the formation of hydroxyl radical under alkaline conditions [73]. Therefore, photocatalytic degradation efficiency was increased. According to the above experiments, the changes in pH have different effects on photocatalysis and adsorption, but the removal rate of MB dyes is similar when pH is between 6 and 10. In order to facilitate study work in the subsequent experiments, the pH 6 with moderate photocatalytic and adsorption properties environment was selected as the experimental condition, unless otherwise specified.

In order to explore whether photocatalytic reaction can completely degrade MB dyes on the adsorbent, GO_3 materials after dark reaction and photoreaction were recovered for the FT-IR test. It can be observed that there are two absorption peaks of BFO at 444 and 555 cm^{-1} from Fig. 11. This may be attributed to the bending and tensile vibrations of Fe–O in FeO_6 octahedral structure of perovskite bismuth ferrite [74]. Besides, new absorption peaks appeared at 1115,

1400, 1624 and 3300–3600 cm^{-1} in the FT-IR spectrum of GO_3. The absorption peak of C-skeleton structure of C–C single bond corresponds to 1115 cm^{-1}. 1400 and 1624 cm^{-1} are the bending vibration of O–H in the hydroxyl group and the stretching vibration of C–OH in –COOH, respectively. It is well known that the broad bands in the range of 3300–3600 cm^{-1} are the stretching vibrations of water and OH groups. These emerging absorption peaks illustrated that GO sheets had been successfully compounded onto pure BFO [75–77]. New absorption peaks of MB dyes appeared on GO_3 nanocomposite after adsorption [78]. The peak at 885 cm^{-1} was related to the rocking vibration of the phenyl ring skeleton plane. Peaks at 1329 and 1245 cm^{-1} correspond to C–N bending and stretching vibrations of N atom attached to the benzene ring, respectively. The peak at 1383 cm^{-1} was related to vibrations of the C–H bond [79, 80]. However, the characteristic peaks of MB disappeared after illumination. It shows that MB can be completely degraded into H_2O and CO_2 by GO_3 through the synergistic effect of photocatalysis and adsorption. No secondary pollution was produced.

In general, adsorption kinetics were used to explain the control mechanism of the adsorption process. To explore the adsorption potential of GO_3 nanocomposite, two commonly applied kinetic models were used to fit the adsorption process as shown in Fig. 12. The models were pseudo-first-order model [Eq. (2)] and pseudo-second-order model [Eq. (3)], respectively [81].
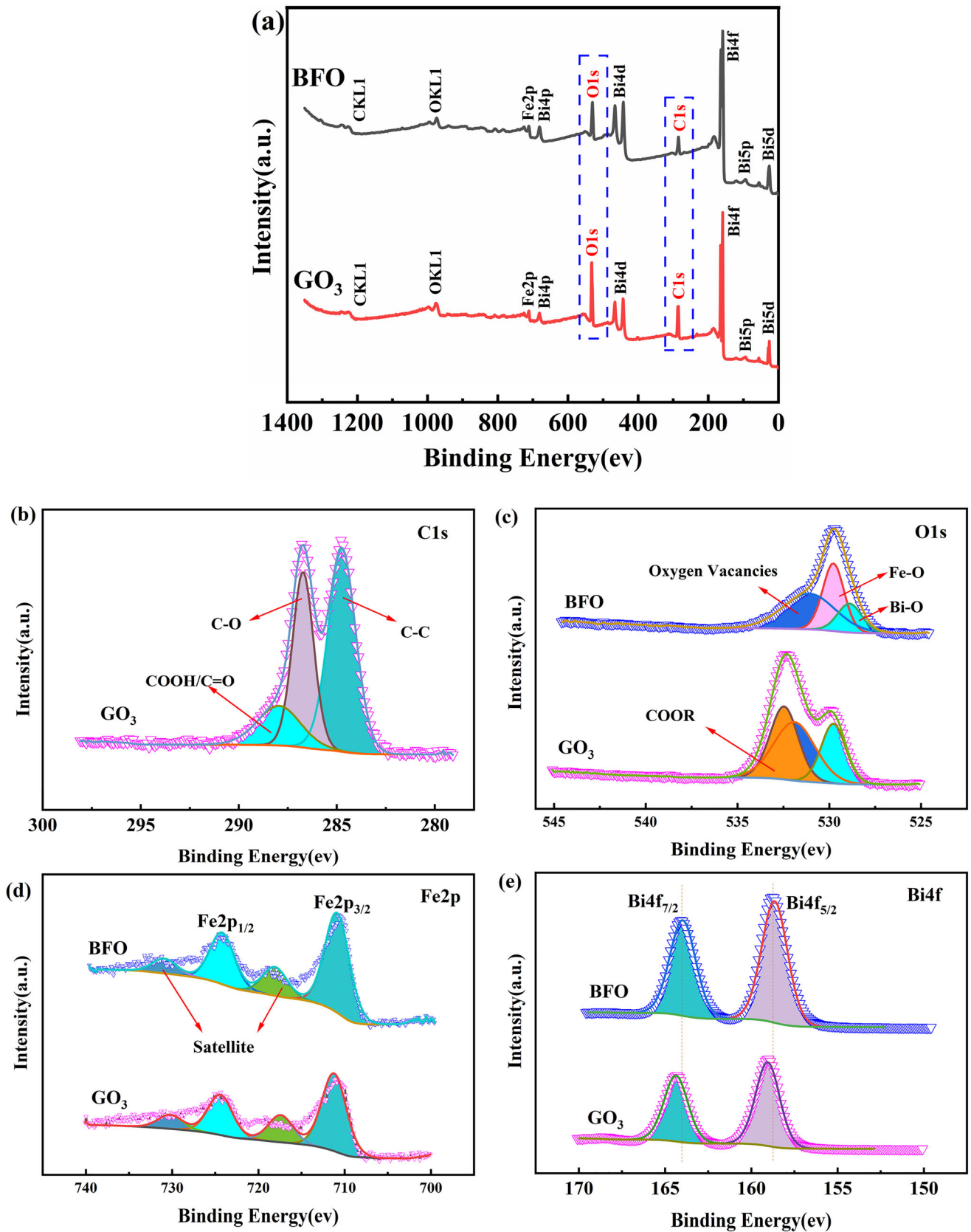
Fig. 7 XPS spectrum of **a** BFO and GO$_3$, and high-resolution XPS spectra of **b** C 1s of GO$_3$, **c** O 1s, **d** Fe 2p and **e** Bi 4f of BFO and GO$_3$
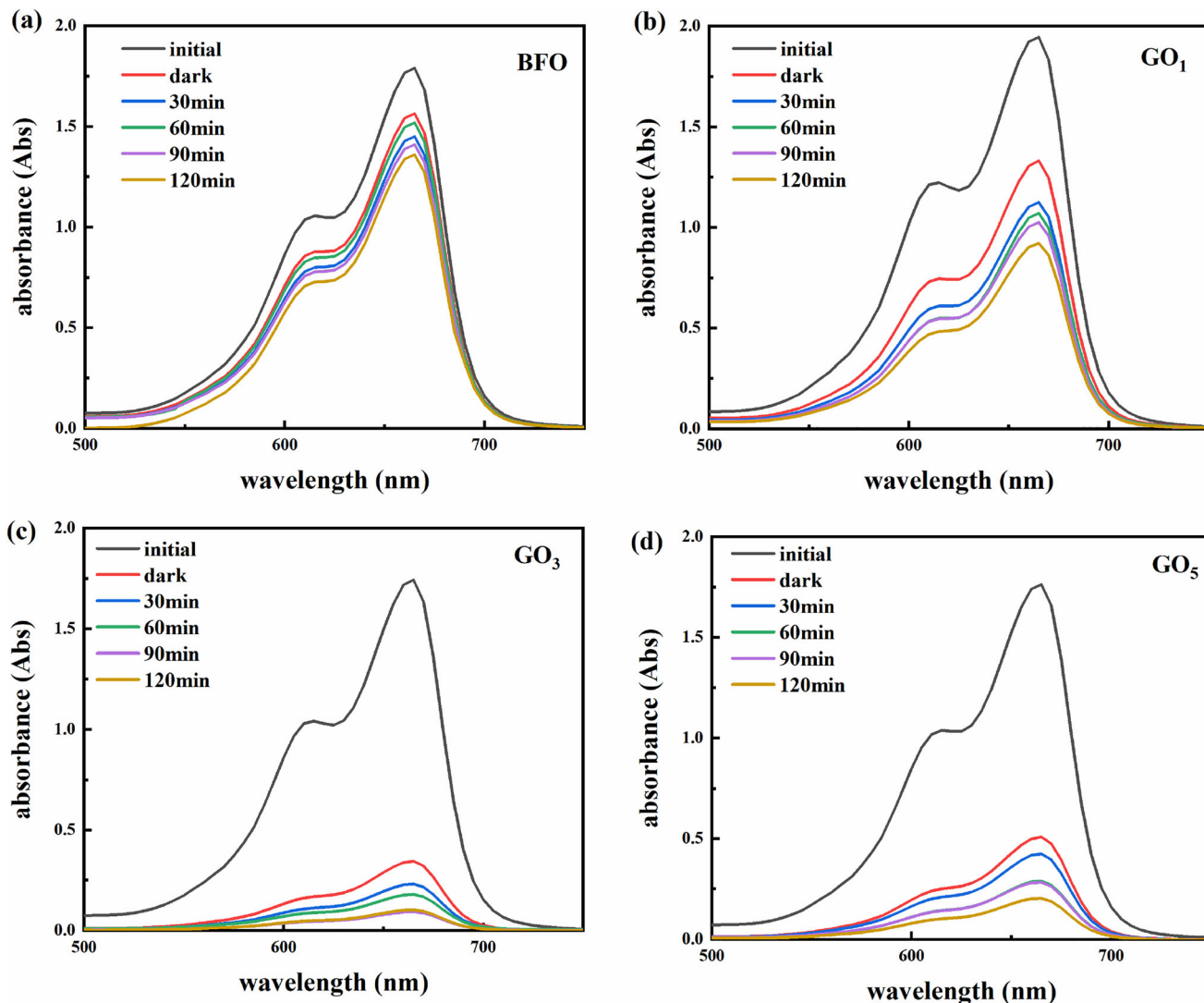
Fig. 8 UV–Vis absorption spectra of **a** BFO, **b** GO_1, **c** GO_3 and **d** GO_5

$$\ln(q_e - q_t) = \ln q_e - k_1 t, \tag{2}$$

$$\frac{t}{q_t} = \frac{1}{k_2 q_e^2} + \frac{t}{q_e}, \tag{3}$$

where q_e is the adsorption capacity at equilibrium (mg/g); q_t is the adsorption capacity at time t (mg/g); k_1 is the pseudo-first-order kinetic rate constant ($\min^{-1}$); k_2 is the pseudo-second-order kinetic rate constant [g·(mg/min)].

The results and related parameters were shown in Fig. 12 and Table 1. It can be seen from Fig. 12 that the adsorption amount of MB dyes increased rapidly during 0–5 min due to the rapid occupation of GO_3 surface active sites. Then the adsorption capacity is gradually increased until the adsorption equilibrium. According to Table 1, a pseudo-second-order kinetic

model had a higher correlation coefficient R^2 than a pseudo-first-order kinetic model. The adsorption of MB for GO_3 sample was more consistent with the correlation coefficient of pseudo-second-order kinetic model. The rate-controlling step of the adsorption process in the pseudo-second-order kinetic model was attributed to chemisorption, which suggested that the adsorption of MB dyes for GO_3 sample was affected by the chemisorption mechanism [82].

Adsorption isotherm models are used to determine the interactions between adsorbents and adsorbates [83]. Energy-homogeneous monolayer adsorption and heterogeneous adsorption on the surface of GO_3 nanocomposites can be predicted by Langmuir isotherm (Eq. (4)) [84] and Freundlich isotherm (Eq. (5)) [85]. The equation can be expressed as:
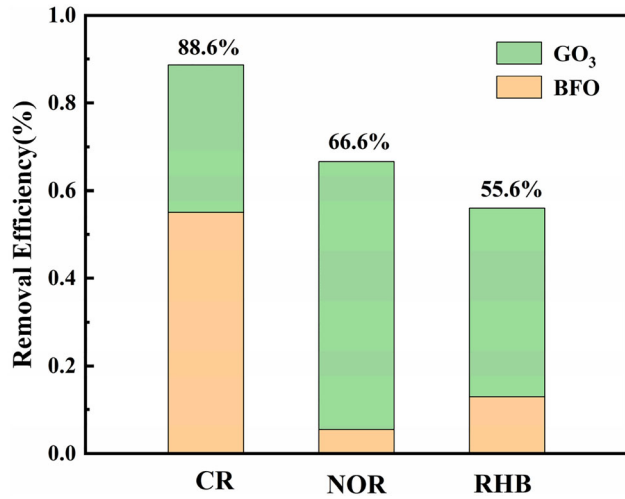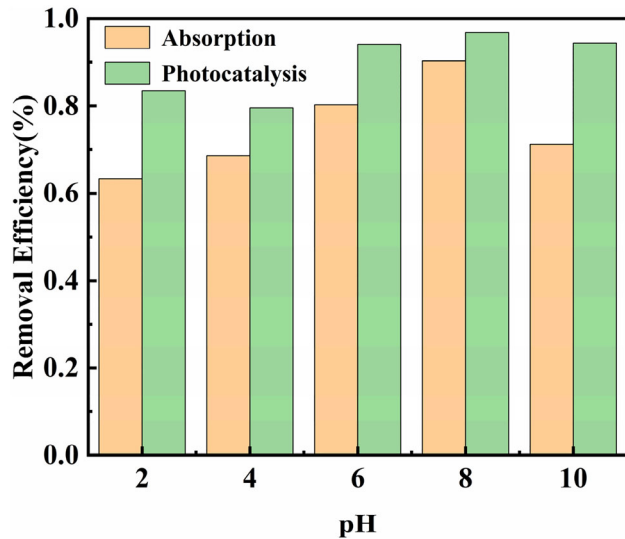
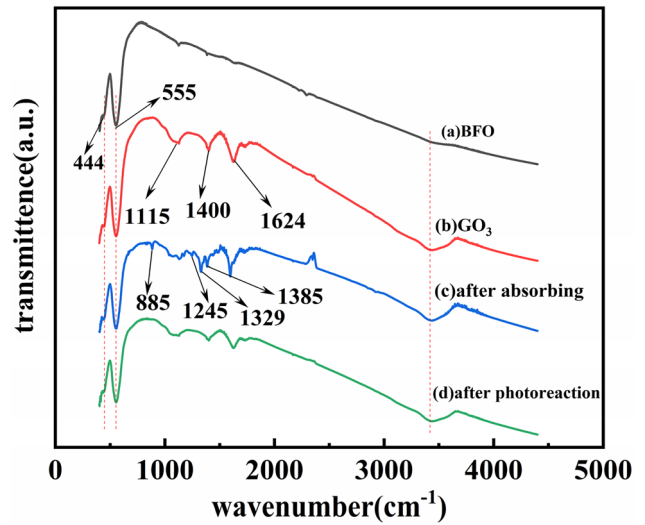Fig. 9 Removal efficiency of CR, NOR and RHB by BFO and GO$_3$

Fig. 11 FT-IR spectra of (a) BFO, (b) GO$_3$, (c) after absorbing, and (d) after photoreaction

Table 2. It can be seen that the experimental data were fitted well with the Langmuir model ($R^2 = 0.98578$) from Fig. 13 and Table 2. According to the Langmuir model, the maximum adsorption capacity would reach 54.177 mg/g when the adsorption could reach equilibrium. The Langmuir isotherm model was based on the assumption that adsorption occurs at equivalently homogeneous sites. Therefore, this experiment supports a monolayer homogeneous adsorption of MB dyes on GO$_3$ sample [86]. The adsorption isotherm process was also examined using the dimensionless separation factor (R_L), and these values were calculated using the following equation:

$$R_L = 1/(1 + K_L C_e), \tag{6}$$

where C_e is the equilibrium mass concentration of adsorbent in solution. Value of R_L determines the favorability of an adsorption process. The adsorption process is favorable when $0 < R_L < 1$, adsorption is not acceptable if $R_L > 1$, the adsorption process is irreversible in nature when $R_L = 0$. In this study, calculated R_L results were all in the range of 0–1, so the adsorption of MB dyes for GO$_3$ sample is a favorable process [63].

The electrons in the valence band (VB) of BFO are excited and moved to the conduction band (CB) under visible light irradiation, producing holes in VB and electrons in CB [87, 88]. Holes and electrons can generate various reactive oxygen species (ROS), such as hydroxyl radicals (˙OH) and superoxide anions

Fig. 10 Removal efficiency of different pH on adsorption and photocatalysis for GO$_3$ sample

$$q_e = q_m K_L \rho_e/(1 + K_L \rho_e), \tag{4}$$

$$q_e = K_F \rho_e^{1/n}, \tag{5}$$

where ρ_e, q_e and q_m are the adsorption equilibrium concentration (mg/g), the adsorption capacity at equilibrium (mg/g) and maximum adsorption capacity, respectively. K_L, K_F and n are the Langmuir constant (L/mg), the Freundlich constant (mg/g) and the Freundlich index, respectively.

Figure 13a and b showed the Freundlich and Langmuir isotherms of MB dye adsorption on GO$_3$ sample, respectively. The key parameters calculated by Langmuir and Freundlich models were listed in
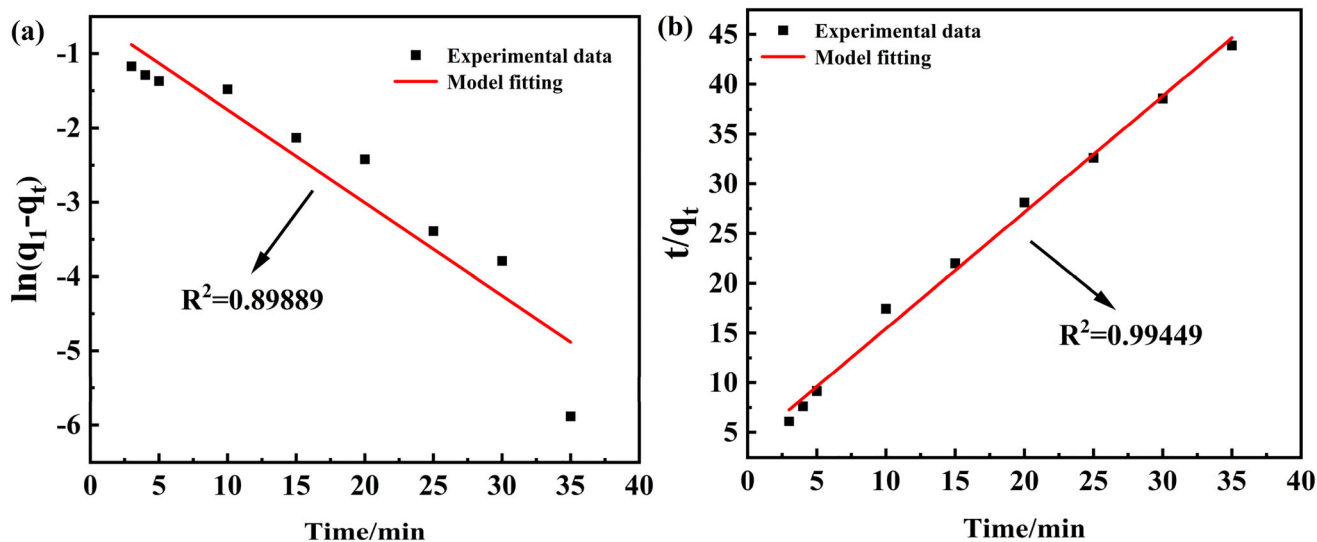
Fig. 12 **a** Pseudo-first-order and **b** pseudo-second-order models of MB adsorption process for GO$_3$ sample

Table 1 Adsorption kinetics parameters of MB adsorption for GO$_3$ sample	Pseudo-first-order model			Pseudo-second-order model		
	k_1 (min^{-1})	Q_e (mg/g)	R^2	k_2 (g·(mg/min))	Q_e (mg/g)	R^2
	0.60450	0.70427	0.89889	0.31018	0.85593	0.99449

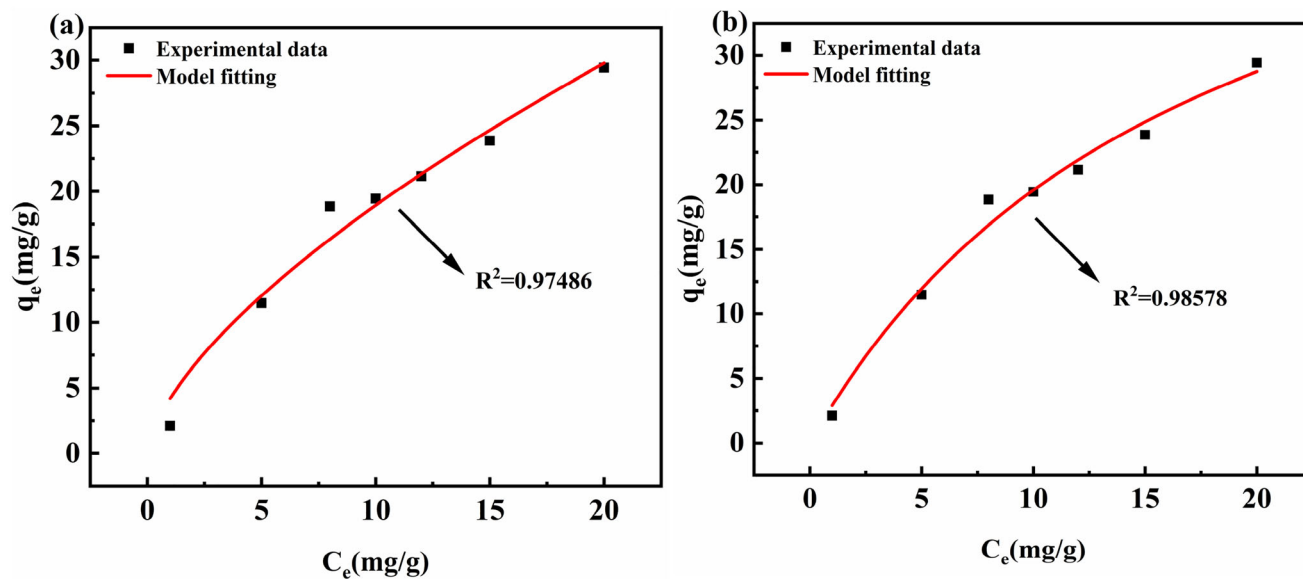**Fig. 13** **a** Freundlich isotherm plots and **b** Langmuir isotherm plots models of MB adsorption process for GO$_3$ sample

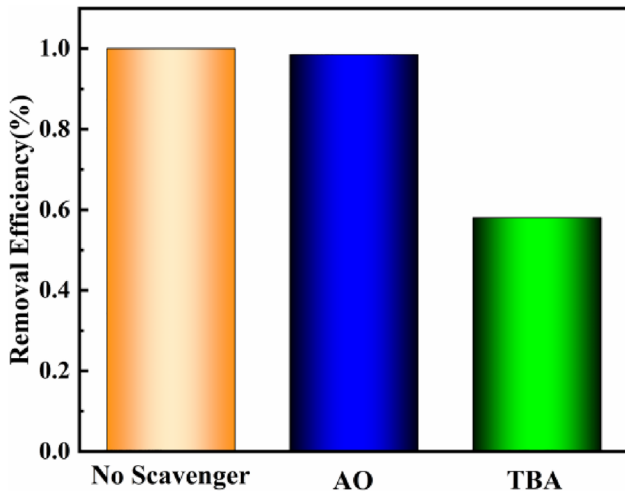| Table 2 Adsorption isotherm parameters of MB adsorption for GO$_3$ sample	Langmuir			Freundlich		
	q_{max} (mg/g)	K_L (L/mg)	R^2	K_F (L/mg)	n	R^2
	54.17700	0.05600	0.98578	4.20100	1.52968	0.97486

Fig. 14 Effect of different scavengers on degradation of MB for GO$_3$ sample

($^{\cdot}$O^{2-}), which can completely degrade organic pollutants into CO$_2$ and H$_2$O [89]. According to the obtained band gap results, the VB potential (E_{VB}) and CB potential (E_{CB}) of GO$_3$ catalyst can be calculated from Eqs. (7) and (8) [90].

$$E_{VB} = X - E^e + 0.5E_g, \tag{7}$$

$$E_{CB} = X - E^e - 0.5E_g. \tag{8}$$

Here X is absolute electronegativity, E^e is the energy of free-electrons under the standard hydrogen electrode (4.5 eV), E_g is the band gap (1.9 eV) of GO$_3$ sample. X value of BFO is 5.93 eV.

According to the Eqs. (7) and (8), E_{CB} of GO$_3$ photocatalyst was 0.48 eV and E_{VB} was 2.38 eV. Since E_{CB} of GO$_3$ was higher than the oxidation potential of O$_2$, generating directly $^{\cdot}$O^{2-} was to be an impossibility (e$^-$ + O$_2$ → $^{\cdot}$O^{2-}, $^{\cdot}$O^{2-} + 2H$^+$ → H$_2$O$_2$, H$_2$O$_2$ + e$^-$ → $^{\cdot}$OH + OH$^-$) [91]. Then, h$^+$ and $^{\cdot}$OH may play a major role in photocatalytic process. To identify the main active species during the photocatalytic degradation of MB dyes for GO$_3$ sample, 1 mmol of AO and 1 mL of TBA were employed to quench h$^+$ and $^{\cdot}$OH radicals, respectively. As shown in Fig. 14, the photocatalytic degradation efficiency was not changed significantly after adding AO, which indicates that h$^+$ does not directly degrade pollutants. After adding TBA, the photocatalytic efficiency was decreased by 42%, which indicated that $^{\cdot}$OH played a major role in photocatalytic degradation process. The photocatalytic mechanism was shown in Fig. 15 and Eqs. (9)–(12). GO$_3$ nanocomposites were irradiated with visible light to generate e$^-$ and h$^+$. $^{\cdot}$OH radicals were generated by the reaction of e$^-$ and h$^+$ with other substances in water, which degraded MB dyes to CO$_2$ and H$_2$O.
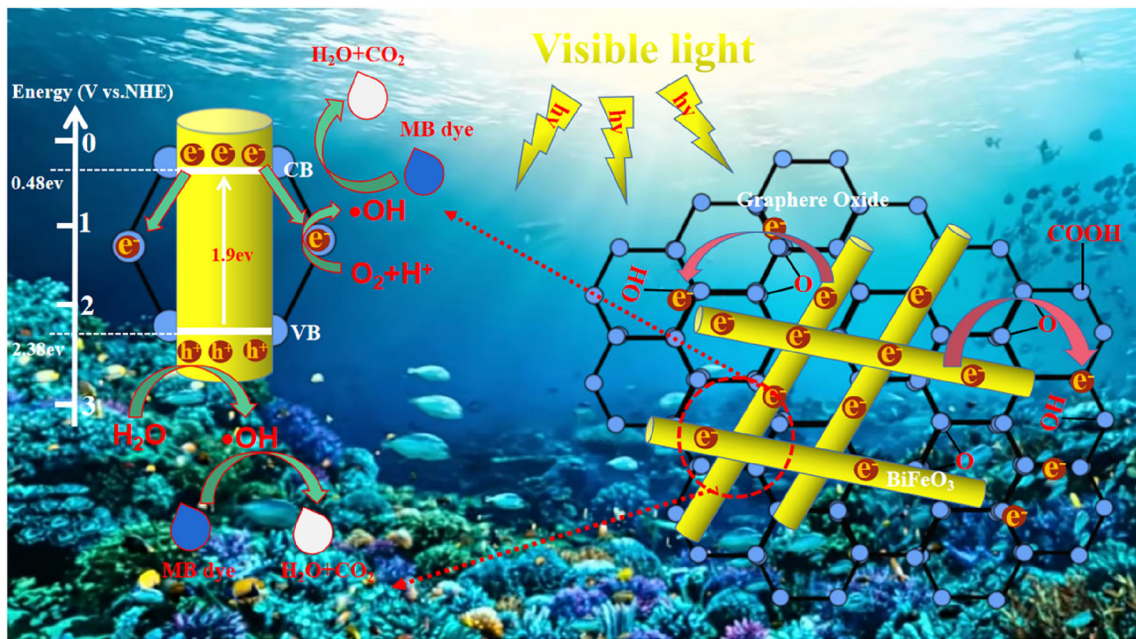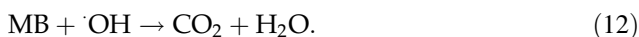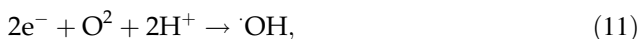

Fig. 15 Mechanism diagram of photocatalysis for GO$_3$ sample

$$GO_3 + hv \rightarrow (e^- + h^+), \tag{9}$$

$$H_2O + h^+ \rightarrow \cdot OH, \tag{10}$$

$$2e^- + O^2 + 2H^+ \rightarrow \cdot OH, \tag{11}$$

$$MB + \cdot OH \rightarrow CO_2 + H_2O. \tag{12}$$

4   Conclusion

$BiFeO_3$@GO nanocomposite had been prepared by electrospinning and ultrasound method. XRD, SEM, TEM, XPS and FT-IR tests proved that GO sheets had been successfully recombined on $BiFeO_3$ nanofibers. The analysis results indicated that GO_3 nanocomposite showed a higher optical absorption capacity and photocatalytic dyes degradability than pure BFO sample. The removal rates of MB, CR, RHB, and NOR dyes by GO_3 nanocomposite were 94.0%, 88.6%, 66.6%, and 55.6%, respectively. Moreover, $BiFeO_3$@GO nanocomposite have lower band gaps (1.9 eV for GO_3), which are more favorable for photocatalytic reactions. FT-IR analysis confirmed the complete degradation of dye pollutants under the synergistic effect of photocatalytic and adsorption for GO_3 sample. O and C elements were increased in GO_3 compared with pure BFO. Bi and Fe elements exist in the form of an oxidation state, and the valence state is $+ 3$. The results not only illustrate the superiority of $BiFeO_3$@GO composite over pure BFO, but also open up a new approach to achieving efficient degradation of dyes.

Author contributions

ZD: Conceptualization, Methodology, Funding acquisition, Writing original draft and analyze experimental results. YL: Data curation, Writing original draft preparation, Investigation. WW: Visualization, Validation. JY: Supervision. LH: Software. DK and FY: Writing reviewing and editing, Funding acquisition, Project administration.

Funding

Data availability

The data that support the findings of this study are available from the corresponding author upon reasonable request, or within the article.

Declarations

Conflict of interest   The authors declare that they have no conflict of interest.

References

1.   H. Alijani, M. Abdouss, H. Khataei, Efficient photocatalytic degradation of toxic dyes over $BiFeO_3$/CdS/rGO nanocomposite under visible light irradiation. Diam. Relat. Mater. **122**, 108817 (2022)

2.   A. Mark, Science and technology for water purification in the coming decades. Nature **452**, 301–310 (2008)

3.   H. Huang, J. Liu, H. Liu, F. Evrendilek, G. Zhang, Y. He, Turning the co-combustion synergy of textile dyeing sludge and waste biochar into emission-to-bottom slag pollution controls toward a circular economy. Renew. Energy **194**, 760–777 (2022)

4.   F. Mushtaq, X. Chen, M. Hoop, H. Torlakcik, E. Pellicer, J. Sort, C. Gattinoni, B.J. Nelson, S. Pané, Piezoelectrically enhanced photocatalysis with $BiFeO_3$ nanostructures for efficient water remediation. i-Science **4**, 236–246 (2018)

5.   E. Brillas, C.A. Martínez-Huitle, Decontamination of wastewaters containing synthetic organic dyes by electrochemical methods, an updated review. Appl. Catal. B **166**, 603–643 (2015)

6.   F. Uddin, Environmental hazard in textile dyeing wastewater from local textile industry. Cellulose **28**, 10715–10739 (2021)

7.   S. Sutar, P. Patil, J. Jadhav, Recent advances in biochar technology for textile dyes wastewater remediation: a review. Environ. Res. **209**, 112841 (2022)

8.   A. Kongor, M. Panchal, M. Athar, M. Vora, B. Makwana, P.C. Jha, V. Jain, Calix [4] pyrrole stabilized PdNPs as an efficient heterogeneous catalyst for enhanced degradation of water-soluble carcinogenic Azo dyes. Catal. Lett. **151**, 548–558 (2021)

9.   J. Xiang, X. Wang, M. Ding, X. Tang, S. Zhang, X. Zhang, Z. Xie, The role of lateral size of MXene nanosheets in

membrane filtration of dyeing wastewater: membrane characteristic and performance. Chemosphere **294**, 133728 (2022)

10. L. Xu, K. Zhao, J. Miao, Z. Yang, Z. Li, L. Zhao, H. Su, L. Lin, Y. Hu, High-strength and anti-bacterial BSA/carboxymethyl chitosan/silver nanoparticles/calcium alginate composite hydrogel membrane for efficient dye/salt separation. Int. J. Biol. Macromol. **22**, 267–2790 (2022)

11. M.J. Uddin, R.E. Ampiaow, W. Lee, Adsorptive removal of dyes from wastewater using a metal–organic framework: a review. Chemosphere **284**, 131314 (2021)

12. J. Mohanta, R. Kumari, M.A. Qaiyum, D. Banashree, D. Soumen, Alkali assisted hydrophobic reinforcement of coconut fiber for enhanced removal of cationic dyes: equilibrium, kinetics, and thermodynamic insight. Int. J. Phytoremediat. **23**, 1423–1431 (2021)

13. S. Asha, C. Hentry, M.R. Bindhu, A.M. Al-Mohaimeed, M.R.A. Gawwad, M.S. Elshikh, Improved photocatalytic activity for degradation of textile dyeing waste water and thiazine dyes using $PbWO_4$ nanoparticles synthesized by co-precipitation method. Environ. Res. **200**, 111721 (2021)

14. S. Miao, H. Xia, H. Gao, X. Mao, M. Shi, Y. Zhang, Metal–organic frameworks-derived CoFeN-NC materials with the enhanced catalytic activity and selectivity for the degradation of organic dyes via adsorption and heterogeneous photo-Fenton. Appl. Surf. Sci. **601**, 154028 (2022)

15. J. Zhong, B. Yang, Y. Feng, Y. Chen, L. Wang, W. You, G. Ying, Enhanced photo-Fenton removal efficiency with core–shell magnetic resin catalyst for textile dyeing wastewater treatment. Water **13**, 968 (2021)

16. S. Ihaddaden, D. Aberkane, A. Boukerroui, D. Robert, Removal of methylene blue (basic dye) by coagulation–flocculation with biomaterials (bentonite and *Opuntia ficus indica*). J. Water Process. Eng. **49**, 102952 (2022)

17. P. Chanikya, P.V. Nidheesh, D.S. Babu, A. Gopinath, M.S. Kumar, Treatment of dyeing wastewater by combined sulfate radical based electrochemical advanced oxidation and electrocoagulation processes. Sep. Purif. Technol. **25**, 1175704 (2021)

18. X. Tang, T. Wang, S. Zhang, L. Fang, H. Zheng, Enhanced performance of a novel flocculant containing rich fluorine groups in refractory dyeing wastewater treatment: removal mechanisms. Sep. Purif. Technol. **263**, 118411 (2021)

19. K. Guo, B. Gao, J. Wang, J. Pan, Q. Yue, X. Xu, Flocculation behaviors of a novel papermaking sludge-based flocculant in practical printing and dyeing wastewater treatment. Front. Environ. Sci. Eng. **15**, 1–11 (2021)

20. W. Xiao, X. Jiang, X. Liu, Z.N. Garba, I. Lawan, L. Wang, Z. Yuan, Adsorption of organic dyes from wastewater by metal-doped porous carbon materials. J. Clean. Prod. **284**, 124773 (2021)

21. A.D. Marczewska, D. Sternik, A. Swiatkowski, K. Kusmierek, W. Gac, B. Buczek, Adsorption of phenol from aqueous and cyclohexane solutions on activated carbons with differentiated surface chemistry. Thermochim. Acta **715**, 179299 (2022)

22. D. Liu, W. Gu, L. Zhou, L. Wang, J. Zhang, Y. Liu, J. Lei, Recent advances in MOF-derived carbon-based nanomaterials for environmental applications in adsorption and catalytic degradation. Chem. Eng. J. **427**, 131503 (2022)

23. M. Sultana, M.H. Rownok, M. Sabrin, M.H. Rahaman, S.M.N. Alam, A review on experimental chemically modified activated carbon to enhance dye and heavy metals adsorption. Clean. Eng. Technol. **6**, 100382 (2022)

24. Y. Chen, Z. Xiang, D. Wang, J. Kang, H. Qi, Effective photocatalytic degradation and physical adsorption of methylene blue using cellulose/GO/TiO_2 hydrogels. R. Soc. Chem. **10**, 23936–23943 (2020)

25. F. Mustafanejad, N. Sajjadi, R. Marandi, M. Zaeimdar, Efficient removal of crystal violet by sulphonic-modified multi-walled carbon nano-tube and graphene oxide. Nanotechnol. Environ. Eng. **6**, 1–9 (2021)

26. S. Liu, M. Pan, Z. Feng, Y. Qin, Y. Wang, L. Tan, T. Sun, Ultra-high adsorption of tetracycline antibiotics on garlic skin-derived porous biomass carbon with high surface area. N. J. Chem. **44**, 1097–1106 (2020)

27. S. Lu, Y. Ma, L. Zhao, Production of ZnO–CoO_x–CeO_2 nanocomposites and their dye removal performance from wastewater by adsorption–photocatalysis. J. Mol. Liq. **364**, 119924 (2022)

28. P. Ding, H. Ji, P. Li, Q. Liu, Y. Wu, M. Guo, Z. Zhou, S. Gao, W. Xu, W. Liu, Q. Wang, S. Chen, Visible-light degradation of antibiotics catalyzed by titania/zirconia/graphitic carbon nitride ternary nanocomposites: a combined experimental and theoretical study. Appl. Catal. B **300**, 12063 (2022)

29. A.A. Elhakim, M. El-Kemary, M.M. Ibrahim, I.M. El-Mehasseb, Direct Z-scheme of WO_3/GO decorated with silver nanoparticles for synergetic adsorption and photocatalytic activity for organic and inorganic water pollutants removal. Appl. Surf. Sci. **564**, 150410 (2021)

30. A. Khlyustova, N. Sirotkin, T. Kusova, A. Kraev, V. Titov, A. Agafonov, Doped TiO_2: the effect of doping elements on photocatalytic activity. R. Soc. Chem. **1**, 1193–1201 (2020)

31. S. Ulag, C. Kalkandelen, T. Bedir, G. Erdemir, S.E. Kuruca, F. Dumludag, C.B. Ustundag, E. Rayaman, N. Ekren, B. Kilic, O. Gunduz, Fabrication of three-dimensional PCL/$BiFeO_3$ scaffolds for biomedical applications. Mater. Sci. Eng. B **261**, 114660 (2020)

32. A. Haruna, I. Abdulkadir, S.O. Idris, Photocatalytic activity and doping effects of $BiFeO_3$ nanoparticles in model organic dyes. Heliyon **6**, e03237 (2020)

33. K.R.P. Anil, S.V.P. Vattikuti, K.K. Mandari, C. Manvitha, S.M.V. Phanikrishna, D.K. Valluri, C. Byon, Bismuth oxide cocatalyst and copper oxide sensitizer in $Cu_2O/TiO_2/Bi_2O_3$ ternary photocatalyst for efficient hydrogen production under solar light irradiation. Ceram. Int. **10**, 11783–11791 (2018)

34. S.M. Lam, J.C. Sin, A.R. Mohamed, A newly emerging visible light-responsive $BiFeO_3$ perovskite for photocatalytic applications: a mini review. Mater. Res. Bull. **90**, 15–30 (2017)

35. S. Lan, C. Yu, F. Sun, Y. Chen, D. Chen, W. Mai, M. Zhu, Tuning piezoelectric driven photocatalysis by La-doped magnetic $BiFeO_3$-based multiferroics for water purification. Nano Energy **93**, 106792 (2022)

36. S. Ali, M. Humayun, W. Pi, Y. Yuan, M. Wang, A. Khan, P. Yue, L. Shu, Z. Zheng, Q. Fu, W. Luo, Fabrication of $BiFeO_3$-g-C_3N_4-WO_3 Z-scheme heterojunction as highly efficient visible-light photocatalyst for water reduction and 2, 4-dichlorophenol degradation: Insight mechanism. J. Hazard. Mater. **397**, 122708 (2020)

37. B. Caglar, E.K. Guner, K.V. Özdokur, A.O. Özdemir, F. İçer, S. Caglar, B. Doğan, B.M. Beşer, Ç. Çırak, A. Tabak, S. Ersoy, Application of $BiFeO_3$ and $Au/BiFeO_3$ decorated kaolinite nanocomposites as efficient photocatalyst for degradation of dye and electrocatalyst for oxygen reduction reaction. J. Photochem. Photobiol. A **428**, 113400 (2021)

38. H. Song, J. Liu, B. Liu, J. Wu, H. Cheng, F. Kang, Two-dimensional materials for thermal management applications. Joule **2**, 442–463 (2018)

39. J. Song, K. Ma, T. Jiao, X. Li, K. Xu, Z. Wang, Preparation and self-assembly of graphene oxide–dye composite Langmuir films: nanostructures and aggregations. Colloids Surf. A **529**, 793–800 (2017)

40. Z. Wang, Y. Jia, W. Song, X. Li, K. Xu, Z. Wang, Optimization of boron adsorption from desalinated seawater onto UiO-66-NH_2/GO composite adsorbent using response surface methodology. J. Clean. Prod. **300**, 126974 (2021)

41. S. Phang, L. Tan, Recent advances in carbon quantum dot (CQD)-based two dimensional materials for photocatalytic applications. Catal. Sci. Technol. **9**, 5882–5905 (2019)

42. K. Sharma, V. Dutta, S. Sharma, P. Raizada, A. Hosseini-Bandegharaei, P. Thakur, P. Singh, Recent advances in enhanced photocatalytic activity of bismuth oxyhalides for efficient photocatalysis of organic pollutants in water: a review. J. Ind. Eng. Chem. **78**, 1–20 (2019)

43. D. Zhang, J. Yang, G. Qiao, J. Wang, H. Li, Facile two-step synthesis of nanofiber polyaniline/graphene/cuprous oxide composite with enhanced photocatalytic performance. Appl. Nanosci. **11**, 983–993 (2021)

44. M.-A. Abbasi, K.M. Amin, M. Ali, Z. Ali, M. Atif, W. Ensinger, W. Khalid, Synergetic effect of adsorption–photocatalysis by GO–CeO_2 nanocomposites for photodegradation of doxorubicin. J. Environ. Chem. Eng. **10**, 107078 (2022)

45. P. Suresh, S. Srinath, Effect of synthesis route on the multiferroic properties of $BiFeO_3$: a comparative study between solid state and sol-gel methods. J. Alloys Compd. **649**, 843–850 (2015)

46. C. Chen, J. Her, T. Pan, Structural and electrical properties of the sol–gel derived multiferroic $BiFeO_3$ monolayer and $NiTiO_3$–$BiFeO_3$ bilayer thin films. Ceram. Int. **46**, 13219–13224 (2020)

47. F. Noori, A. Gholizadeh, Structural, optical, magnetic properties and visible light photocatalytic activity of $BiFeO_3$/-graphene oxide nanocomposites. Mater. Res. Express **6**, 1250g1 (2019)

48. M. Ait-Tamerd, B. Abraime, A. Kadiri, A. Lahmar, M. El-Marssi, M. Hamedoun, A. Benyoussef, A. El-Kenz, Prediction of magnetoelectric properties of defect $BiFeO_3$ thin films using Monte Carlo simulations. J. Magn. Magn. Mater. **539**, 168402 (2021)

49. T. Kumar-Dixit, S. Sharma, A.S.K. Sinha, Development of heterojunction in N-rGO supported bismuth ferrite photocatalyst for degradation of Rhodamine B. Inorg. Chem. Commun. **117**, 107945 (2020)

50. Z. Li, L. Cheng, S. Zhang, Z. Wang, C. Fu, Enhanced photocatalytic and magnetic recovery performance of Co-doped $BiFeO_3$ based on MOFs precursor. J. Solid State Chem. **279**, 120978 (2019)

51. M. Abushad, W. Khan, S. Naseem, S. Husain, M. Nadeem, A. Ansari, Influence of Mn doping on microstructure, optical, dielectric and magnetic properties of $BiFeO_3$ nanoceramics synthesized via sol–gel method. Ceram. Int. **45**, 7437–7445 (2019)

52. C. Wang, S. Gao, J. Zhu, X. Xia, M. Wang, Y. Xiong, Enhanced activation of peroxydisulfate by strontium modified $BiFeO_3$ perovskite for ciprofloxacin degradation. J. Environ. Sci. **99**, 249–259 (2021)

53. C. Chen, J. Cheng, S. Yu, L. Che, Z. Meng, Hydrothermal synthesis of perovskite bismuth ferrite crystallites. J. Cryst. Growth **291**, 135–139 (2006)

54. M. Sakar, S. Balakumar, Reverse Ostwald ripening process induced dispersion of Cu_2O nanoparticles in silver-matrix and their interfacial mechanism mediated sunlight driven photocatalytic properties. J. Photochem. Photobiol. A **356**, 150–158 (2018)

55. K.A. Rosowski, E. Vidal-Henriquez, D. Zwicker, W.S. Robert, E.R. Dufresne, Elastic stresses reverse Ostwald ripening. Soft Matter **16**, 5892–5897 (2020)

56. S. Bharathkumar, M. Sakar, J. Archana, M. Navaneethan, S. Balakumar, Interfacial engineering in 3D/2D and 1D/2D

bismuth ferrite (BiFeO$_3$)/graphene oxide nanocomposites for the enhanced photocatalytic activities under sunlight. Chemosphere **284**, 131280 (2021)

57. Y. Tie, S. Ma, S. Pei, Q. Zhang, K. Zhu, R. Zhang, X. Xu, T. Han, W. Liu, Pr doped BiFeO$_3$ hollow nanofibers via electrospinning method as a formaldehyde sensor. Sens. Actuator B **308**, 127689 (2020)

58. T. Soltani, B.K. Lee, Sono-synthesis of nanocrystallized BiFeO$_3$/reduced graphene oxide composites for visible photocatalytic degradation improvement of bisphenol A. Chem. Eng. J. **306**, 204–213 (2016)

59. T. Wang, T. Xu, S. Gao, S. Song, Effect of Nd and Nb co-doping on the structural, magnetic and optical properties of multiferroic BiFeO$_3$ nanoparticles prepared by sol–gel method. Ceram. Int. **45**, 4489–4495 (2017)

60. Y. Si, Y. Xia, S. Shang, X. Xiong, X. Zeng, J. Zhou, Y. Li, Enhanced visible light driven photocatalytic behavior of BiFeO$_3$/reduced graphene oxide composites. Nanomaterials **8**, 526 (2018)

61. B.S. Goud, G. Koyyada, J.H. Jung, G.R. Reddy, J. Shim, N.D. Nam, S.V.-P. Vattikuti, Surface oxygen vacancy facilitated Z-scheme MoS$_2$/Bi$_2$O$_3$ heterojunction for enhanced visible-light driven photocatalysis-pollutant degradation and hydrogen production. Int. J. Hydrog. Energy **45**, 18961–18975 (2020)

62. E. Shang, Y. Li, J. Niu, S. Li, G. Zhang, X. Wang, Photocatalytic degradation of perfluorooctanoic acid over Pb–BiFeO$_3$/rGO catalyst: Kinetics and mechanism. Chemosphere **211**, 34–43 (2018)

63. D. Mohtaram, S.A. Mohammad, A. Iftekhar, Z.A.W. Murad, R. Ziyaur, M. Mohammad, Highly efficient and stable Fe$_2$O$_3$/g-C$_3$N$_4$/GO nanocomposite with Z-scheme electron transfer pathway: role of photocatalytic activity and adsorption isotherm of organic pollutants in wastewater. Appl. Surf. Sci. **604**, 154604 (2022)

64. J.H. Shah, A.S. Malik, A.M. Idris, S. Rasheed, H. Han, Intrinsic photocatalytic water oxidation activity of Mn-doped ferroelectric BiFeO$_3$. Chin. J. Catal. **42**, 945–952 (2021)

65. L. Di, H. Yang, T. Xian, X. Chen, Facile synthesis and enhanced visible-light photocatalytic activity of novel p-Ag$_3$PO$_4$/n-BiFeO$_3$ heterojunction composites for dye degradation. Nanoscale Res. Lett. **13**, 257 (2018)

66. S.V.P. Vattikuti, K.C. Devarayapalli, N.N.K. Reddy, T.N. Nguyen, N.N. Dang, J. Shim, Onion-ring-like carbon and nitrogen from ZIF-8 on TiO$_2$/Fe$_2$O$_3$ nanostructure for overall electrochemical water splitting. J. Phys. Chem. Lett. **25**, 5909–5918 (2021)

67. C. Álvarez-Esmorís, L. Rodríguez-López, A. Núñez-Delgado, E. Álvarez-Rodríguez, D. Fernández-Calviño, M. Arias-Estévez, Influence of pH on the adsorption–desorption of doxycycline, enrofloxacin, and sulfamethoxypyridazine in soils with variable surface charge. Environ. Res. **214**, 114071 (2022)

68. F. Yang, X. Yu, Z. Liu, K. Wang, Y. Liang, J. Qiu, T. Zhang, J. Niu, J. Zhao, B. Yao, The effects of pH on reactive species formation in moxifloxacin photocatalytic degradation via BiPO$_4$ prismatic. Opt. Mater. **133**, 112892 (2022)

69. M.A. Hassan, M.R. El-Aassar, M.A. El-Hashemy, M.A. Betiha, M. Alzaid, A.N. Alqhobisi, L.A. Alzarea, I.H. Alsohaimi, Sulfanilic acid-functionalized magnetic GO as a robust adsorbent for the efficient adsorption of methylene blue from aqueous solution. J. Mol. Liq. **361**, 119603 (2022)

70. H.K. Yağmur, İ Kaya, Synthesis and characterization of magnetic ZnCl$_2$-activated carbon produced from coconut shell for the adsorption of methylene blue. J. Mol. Struct. **1232**, 130071 (2021)

71. X. Tang, G. Ran, J. Li, Z. Zhang, C. Xiang, Extremely efficient and rapidly adsorb methylene blue using porous adsorbent prepared from waste paper: kinetics and equilibrium studies. J. Hazard. Mater. **402**, 123579 (2021)

72. Y. Wang, Y. Tang, J. Sun, X. Wu, H. Liang, Y. Qu, L. Jing, BiFeO$_3$/Bi$_2$Fe$_4$O$_9$ S-scheme heterojunction hollow nanospheres for high-efficiency photocatalytic o-chlorophenol degradation. Appl. Catal. B **319**, 121893 (2022)

73. J. Ćirković, A. Radojković, D.L. Golić, N. Tasić, M. Čizmić, G. Branković, Z. Branković, Visible-light photocatalytic degradation of Mordant Blue 9 by single-phase BiFeO$_3$ nanoparticles. J. Environ. Chem. Eng. **9**, 104587 (2021)

74. M. Shahid, S. Bashir, A. Afzal, S. Shamsah, A. Jamil, Synergistic impacts of composite formation and doping techniques to boost the photocatalytic aptitude of the BiFeO$_3$ nanostructure. Ceram. Int. **48**, 2566–2576 (2022)

75. L. Li, Y. Liu, S. Zhang, M. Liang, F. Li, Y. Yuan, Enhanced mineralization of bisphenol A by eco-friendly BiFeO$_3$–MnO$_2$ composite: performance, mechanism and toxicity assessment. J. Hazard. Mater. **399**, 122883 (2020)

76. M. Krishnamoorthy, N.H. Ahmad, H.N. Amran, M.A. Mohamed, N.H.M. Kaus, S.F.M. Yusoff, BiFeO$_3$ immobilized within liquid natural rubber-based hydrogel with enhanced adsorption–photocatalytic performance. Int. J. Biol. Macromol. **182**, 1495–1506 (2021)

77. S. Kumar, R.D. Kaushik, L.P. Purohit, Novel ZnO tetrapod-reduced graphene oxide nanocomposites for enhanced photocatalytic degradation of phenolic compounds and MB dye. J. Mol. Liq. **327**, 114814 (2021)

78. S. Jiao, Y. Zhao, M. Bi, S. Bi, X. Li, B. Wang, C. Li, Y. Dong, Removal of methylene blue from water by BiFeO$_3$/carbon fibre nanocomposite and its photocatalytic regeneration. Catalyst **8**, 267 (2018)

79. Z. Yu, S. Chuang, Probing methylene blue photocatalytic degradation by adsorbed ethanol with in situ IR. J. Phys. Chem. C **111**, 13813–13820 (2007)

80. M. Cheng, G. Zeng, D. Huang, C. Lai, Y. Liu, C. Zhang, R. Wang, L. Qin, W. Xue, B. Song, S. Ye, H. Yi, High adsorption of methylene blue by salicylic acid–methanol modified steel converter slag and evaluation of its mechanism. J. Colloid Interface Sci. **515**, 232–239 (2018)

81. G. Li, J. Li, W. Tan, M. Yang, H. Wang, X. Wang, Effectiveness and mechanisms of the adsorption of carbendazim from wastewater onto commercial activated carbon. Chemosphere **304**, 135231 (2022)

82. Y. He, D. Jiang, J. Chen, D. Jiang, Yu. Zhang, Synthesis of MnO_2 nanosheets on montmorillonite for oxidative degradation and adsorption of methylene blue. J. Colloid Interface Sci. **510**, 207–220 (2018)

83. J. Zhao, R. Boada, G. Cibin, C. Palet, Enhancement of selective adsorption of Cr species via modification of pine biomass. Sci. Total Environ. **756**, 143816 (2021)

84. D. Zhou, G. Xie, X. Hu, X. Cai, Y. Zhao, X. Hu, Q. Jin, X. Fu, X. Tan, C. Liang, K. Lai, H. Wang, C. Tang, Coupling of Kenaf biochar and magnetic $BiFeO_3$ onto cross-linked chitosan for enhancing separation performance and Cr(VI) ions removal efficiency. Int. J. Environ. Res. Public Health **17**, 788 (2020)

85. K. Zare, H. Sadegh, R. Shahryari, M. Asif, I. Tyagi, S. Agarwal, V.K. Gupta, Equilibrium and kinetic study of ammonium ion adsorption by Fe_3O_4 nanoparticles from aqueous solutions. J. Mol. Liq. **213**, 345–350 (2016)

86. H. Zhu, E. Zhu, Y. Xie, D. Liu, Y. Hu, Z. Shi, C. Xiong, Q. Yang, Hydrangea-like nanocellulose microspheres with high dye adsorption and drug encapsulation prepared by emulsion method. Carbohydr. Polym. **296**, 119947 (2022)

87. A. Indriyani, Y. Yulizar, R.T. Yunarti, D.O.B. Apriandanu, R.M. Surya, One-pot green fabrication of BiFeO3 nanoparticles via *Abelmoschus esculentus* L. leaves extracts for photocatalytic dye degradation. Appl. Surf. Sci. **563**, 150113 (2021)

88. S.V.P. Vattikuti, K.R.P. Anil, J. Shim, C. Byon, In situ fabrication of the Bi_2O_3–V_2O_5 hybrid embedded with graphitic carbon nitride nanosheets: oxygen vacancies mediated enhanced visible-light-driven photocatalytic degradation of organic pollutants and hydrogen evolution. Appl. Surf. Sci. **447**, 740–756 (2018)

89. S. Chaiwichian, K. Wetchakun, W. Kangwansupamonkon, N. Wetchakun, Novel visible-light-driven $BiFeO_3$–Bi_2WO_6 nanocomposites toward degradation of dyes. J. Photochem. Photobiol. A **349**, 183–192 (2017)

90. G. Koyyada, B.S. Goud, K.C. Devarayapalli, J. Shim, P. Vattikuti, J.H. Kim, $BiFeO_3$/Fe_2O_3 electrode for photoelectrochemical water oxidation and photocatalytic dye degradation: a single step synthetic approach. Chemosphere **303**, 135071 (2022)

91. Y. Wu, H. Ji, Q. Liu, Z. Sun, P. Li, P. Ding, M. Guo, X. Yi, W. Xu, C. Wang, S. Gao, Q. Wang, W. Liu, S. Chen, Visible light photocatalytic degradation of sulfanilamide enhanced by Mo doping of BiOBr nanoflowers. J. Hazard. Mater. **424**, 127563 (2022)